

Directed Conversion of Alzheimer's Disease Patient Skin Fibroblasts into Functional Neurons

Liang Qiang,^{1,3} Ryouzuke Fujita,^{1,3} Toru Yamashita,^{1,3} Sergio Angulo,^{2,3} Herve Rhinn,¹ David Rhee,¹ Claudia Doege,¹ Lily Chau,¹ Laetitia Aubry,¹ William B. Vanti,¹ Herman Moreno,² and Asa Abeliovich^{1,*}

¹Departments of Pathology, Cell Biology, and Neurology and Taub Institute, Columbia University, Black Building 1208, 650 West 168th Street, New York, NY 10032, USA

²The Robert F. Furchgott Center for Neural and Behavioral Science, Departments of Neurology and Pharmacology and Physiology, State University of New York, Downstate Medical Center, Brooklyn, NY 11203, USA

³These authors contributed equally to this work

*Correspondence: aa900@columbia.edu

DOI 10.1016/j.cell.2011.07.007

SUMMARY

Directed conversion of mature human cells, as from fibroblasts to neurons, is of potential clinical utility for neurological disease modeling as well as cell therapeutics. Here, we describe the efficient generation of human-induced neuronal (hiN) cells from adult skin fibroblasts of unaffected individuals and Alzheimer's patients, using virally transduced transcription regulators and extrinsic support factors. hiN cells from unaffected individuals display morphological, electrophysiological, and gene expression profiles that typify glutamatergic forebrain neurons and are competent to integrate functionally into the rodent CNS. hiN cells from familial Alzheimer disease (FAD) patients with presenilin-1 or -2 mutations exhibit altered processing and localization of amyloid precursor protein (APP) and increased production of A β , relative to the source patient fibroblasts or hiN cells from unaffected individuals. Together, our findings demonstrate directed conversion of human fibroblasts to a neuronal phenotype and reveal cell type-selective pathology in hiN cells derived from FAD patients.

INTRODUCTION

Mature mammalian cells can be reprogrammed to alternative fates by introduction of lineage-specific transcription regulators. For instance, Myod1 expression has been shown to induce a myocyte phenotype in fibroblast cultures (Davis et al., 1987). Similarly, transduction of a set of pluripotency regulators is sufficient to convert skin fibroblasts to induced pluripotency stem (iPS) cells with embryonic stem cell characteristics (Takahashi et al., 2007; Takahashi and Yamanaka, 2006; Yu et al., 2007). iPS cell technology has fueled much excitement in regenerative medicine, as these cells could be differentiated to generate "replace-

ment" cell therapeutics. Patient iPS cell-derived neurons have also been proposed to serve as neurodegenerative disease models (Abeliovich and Doege, 2009).

A limitation to human iPS cell technology is that it remains inefficient (less than 1% of cells are typically reprogrammed) and time intensive; iPS cell generation and subsequent differentiation to a neuronal phenotype can take 1–2 months each. Furthermore, the pluripotent state is associated with tumorigenesis and genetic instability (Pera, 2011). Recently, the directed conversion of rodent skin fibroblasts to a neuronal fate was reported, utilizing a set of three forebrain transcription regulators and apparently circumventing the production of a pluripotent intermediate state (Vierbuchen et al., 2010). Here, we describe the directed conversion of adult human fibroblasts to a neuronal phenotype, termed human-induced neuronal (hiN) cells. To validate the approach, we show that hiN cells display electrophysiological properties of forebrain glutamatergic neurons and can integrate into mammalian CNS circuitry.

We further apply hiN cell technology to a panel of skin fibroblasts derived from patients with sporadic or familial forms of Alzheimer's disease (AD) and examine AD-associated neuronal pathologies. AD patients typically present with age-associated cognitive dysfunction, including reduced short-term (episodic) memory and spatial disorientation. These cognitive deficits are associated with neuronal and synaptic loss that is most prominent within the medial temporal lobe of the cerebral cortex and the hippocampus (Alzheimer, 1907). Additional pathological features of AD include extracellular amyloid plaques composed largely of A β fragments of amyloid precursor protein (APP) and intraneuronal tangles of Tau-paired helical filaments (Hardy and Selkoe, 2002). Rare, autosomal, dominantly inherited familial forms of AD (FAD) are caused by mutations in APP or in the two presenilin genes (presenilin-1 and -2, or PSEN1 and PSEN2) that encode components of the γ -secretase enzyme complex that is required for APP cleavage to A β (Hardy and Selkoe, 2002).

The amyloid hypothesis of AD, which is based on the aforementioned pathological and genetic findings, proposes that modified cleavage of APP by β -secretase and γ -secretase leads

to the generation of a pathogenic A β 42 fragment. Consistent with this hypothesis, expression of disease-associated PSEN FAD mutations in cell and animal models leads to preferential accumulation of A β 42 isoform relative to an A β 40 isoform. Nonetheless, basic questions regarding the pathogenic mechanism of PSEN FAD mutations remain (De Strooper and Annaert, 2010; Shen and Kelleher, 2007). For instance, although PSEN FAD mutations increase relative A β 42 production, they paradoxically reduce total γ -secretase activity, at least in cell-free and heterologous cell overexpression systems (Bentahir et al., 2006; Walker et al., 2005). The potential role of reduced γ -secretase activity in the disease process remains controversial. As the majority of studies to date rely on exogenous overexpression of PSEN FAD mutations in tumor cells, transgenic mice, or skin fibroblasts, the impact of endogenous PSEN FAD mutations on functional human patient neurons remains unclear. Moreover, why mutations in the broadly expressed PSEN-1 and -2 genes lead to a selective neuronal pathology is an open question.

RESULTS

Phenotypic Characterization of hiN Cells

We initially attempted to convert human adult skin fibroblasts (STC0022; see Table S1 available online) to hiN cells by viral cotransduction of a combination of three transcription regulators—*Ascl1*, *Brn2*, and *Myt1l*—that were shown to be effective for reprogramming of rodent cells (Vierbuchen et al., 2010). These attempts were unsuccessful and led to prominent apoptotic cell death. Viral cotransduction of a larger set of forebrain transcription regulators—*Brn2*, *Myt1l*, *Zic1*, *Olig2*, and *Ascl1*, in the presence of neuronal survival factors (including brain-derived neurotrophic factor [BDNF], neurotrophin-3 [NT3], and glial-conditioned media [GCM]), resulted in the generation of cells with a neuronal morphology (human-induced neuronal cells, or hiN cells) (Figures 1A–1N). Three weeks after viral transduction, hiN cells were positive for neuronal markers, including Tuj1, MAP2, Tau1, NeuN, NCAM, and Neurofilament-160 kd (Figures 1B–1G and 1J–1N and Figure S1). Such cells were never observed in fibroblast cultures transduced with control vector only (Figures 1H and 1I). Cell staining with the astroglial marker glial fibrillary acidic protein (GFAP) was not detected in hiN cell cultures (Figure S1). More than 90% of MAP2-positive cells were positive for the neocortical glutamate neuron marker *Tbr1* (Figure 1K), and these *Tbr1*-positive cells did not express the fibroblast marker, fibroblast-specific protein-1 (FSP1; Figure 1L). Approximately half of the MAP2-positive cells were positive for the mature glutamatergic neuron marker vesicular glutamate transporter-1 (vGLUT1) in a stereotypical punctate pattern (Figure 1M). Only rare MAP2-positive cells (less than 1%) displayed the GABAergic neuron marker, glutamic acid decarboxylase-65 (GAD65; Figure 1N).

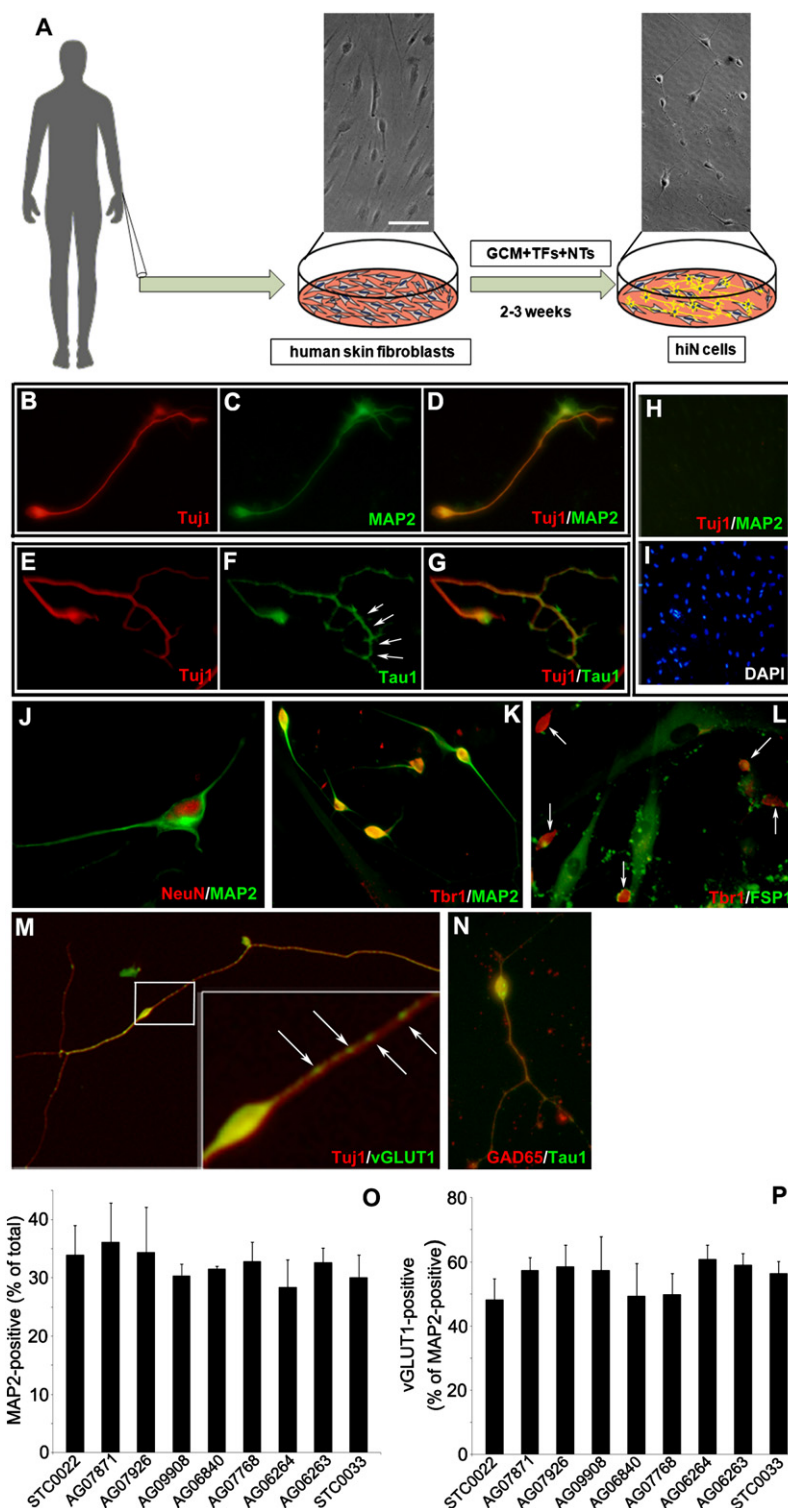
We applied our hiN cell conversion protocol to a panel of nine adult human skin fibroblast lines in total (see Table S1). Quantitative analysis indicates that conversion efficiency of fibroblasts to MAP2-positive hiN cells across these lines ranged from 7.1% to 8.9% (as a percentage of input fibroblasts; n = 3 per group). After accounting for cell attrition during the 3 week culture, 28.4%–36.1% of the surviving cells were MAP2 positive (Fig-

ure 1O). Across these lines, 48.2%–60.9% of the MAP2-positive cells were also positive for vGLUT1 (Figure 1P).

Time course analysis indicated that MAP2- and vGLUT1-positive hiN cells first appear by day 7 after viral vector transduction and that maximal conversion occurs by 21 days (Figure 2A). After 21 days, hiN cell number decreased, and this was accompanied by evidence of apoptosis (Figure 2A and Figures S2C–S2G). Remaining cells displayed progressively elongated processes, as expected (Figure S2B). To determine the minimal factors that are necessary and sufficient to generate hiN cells, we removed individual transcription factor vectors or extrinsic components from the conversion protocol. These data indicated that *Ascl1* and *Brn2* are essential for the process, whereas *Zic1* and *Myt1l* modify efficiency, and *Oligo2* appears to be redundant (Figure 2B). After transduction with viral factor cocktails, converted cells maintained expression of the extrinsic virally encoded *Ascl1*, *Brn2*, and *Myt1l* transcription factors, as determined by RT-PCR analysis, whereas extrinsic *Zic1* expression was maintained only in a subset of cultures (Figure S2A). Maintenance of exogenous factor expression may have contributed to the apoptotic loss of hiN cells with extended culturing. Of the tested soluble extrinsic factors, only BDNF appeared essential for production of MAP2⁺/vGLUT1⁺ cells (Figure 2B and Figure S2D).

A single polycistronic lentivirus vector harboring the genes *Ascl1*, *Brn2*, and *Zic1* (ABZ vector) was sufficient for the conversion process (Figure 2C and Figures S2K–S2N). ABZ vector-mediated conversion was highly efficient and could be further enhanced by adding *Myt1l* (Figure 2C and Figures S2O–S2V). Specifically, 62% \pm 6% of the adult human fibroblasts that were transduced with the ABZ vector and 85% \pm 15% of the cells that were transduced with the ABZ vector and *Myt1l* acquired a MAP2-positive neuronal morphology phenotype (Figure 2C and Figures S2L–S2Q). These hiN cells expressed additional neuron markers, including Tau-1, Tuj1, Tbr1, and vGLUT1 (Figures S2R–S2V).

To further characterize the hiN cell phenotype, we performed whole-transcriptome gene expression profiling on neurons that were purified from hiN cell cultures. hiN cell cultures were subjected to fluorescence-activated cell sorting (FACS; Figures S2H–S2J) to select for neural cell adhesion molecule (NCAM, a marker for mature neurons as well as some neural progenitors)-positive cells. RNA preparations from FACS-purified hiN cells, total (“mixed”) cultures, and unconverted fibroblasts were then analyzed for genome-wide expression (Table S2). Hierarchical clustering analysis demonstrated that the transcriptome profiles of purified hiN cells were more similar to each other than to the originating fibroblasts (Figure 2D). Using gene ontology (GO) functional annotation, we identified genes that are most enriched within the purified hiN cell samples relative to the fibroblast samples (upregulated by at least 4-fold with a significance analyses of microarrays false discovery rate [FDR] cutoff of less than 25%). Consistent with a neuronal phenotype, the most highly enriched, functionally annotated gene sets in the purified hiN samples included “axonal projection” and “neuronal differentiation” genes (Figures 2E–2G and Table S2). Finally, we performed hierarchical clustering to broadly compare hiN cell gene expression profiles to those seen in human neurons (isolated from postmortem brain samples) and



other cell types. As expected, FACS-sorted hiN cell samples clustered most closely with CNS neurons rather than fibroblasts, astrocytes, neural progenitors, or pluripotent ES or iPS cells (Figure S3).

and 3E–3G). Expression of Nestin, which is associated with neuronal progenitors but also functions more generally as a cytoskeleton regulator during morphological cell changes (Gilyarov, 2008), appeared transiently in a subpopulation of cells (<10%;

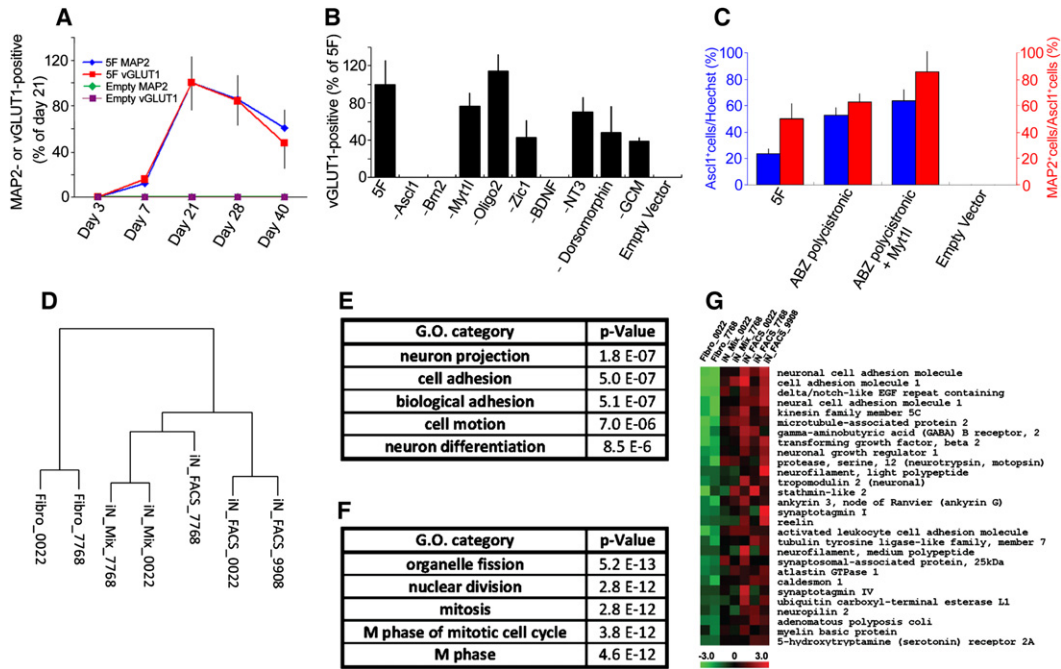


Figure 2. Further Description of hiN Cell Conversion: Essential Factors and Transcriptome Analysis

(A) Temporal profile of hiN cell conversion. MAP2- or vGLUT1-positive cells were quantified at indicated time points after transduction with conversion factor vectors (5F, indicated as blue or red line) or empty vector (Empty, green or purple line). The number of MAP2- (diamond) and vGLUT1-positive (square) cells peaked at 21 days after 5F transduction, whereas such cells were not apparent with empty vector. $n = 3$ at each time point; data are presented as mean \pm SEM. (B) Required factors in hiN cell conversion. Fibroblasts were transduced with the 5-factor (5F) cocktail as above or with factor mixes lacking the indicated individual factors. Bar graphs indicate the number of vGLUT1-positive cells at 3 weeks after transduction, as a percent of 5F transduction. GCM, glial-conditioned media. $n = 3$ per group. Results represent the mean \pm SEM.

(C) Fibroblasts were transduced with a polycistronic vector harboring *Ascl1*, *Bmi2*, and *Zic1* (ABZ-polycistronic) alone or in combination with a *Myt1l* vector. The percentage of *Ascl1*-positive cells per total cell number (Hoechst-positive nuclei, blue bars) reflects the transduction efficiency. The percentage of MAP2-positive hiN cells of transduced *Ascl1*-positive cells (red bars) reflects the hiN cell conversion efficiency. $n = 3$ per group. Results represent the mean \pm SEM.

(D) Dendrogram presenting the hierarchical clustering of gene expression array profiles as measured by Human Genome U133 Plus 2.0 Arrays (Affymetrix). Complete linkage hierarchical clustering analysis was performed using Pearson's correlation metric. The dendrogram includes individual samples from FACS-sorted hiN cells (iN_FACS), unsorted hiN cell cultures (iN_Mix), or the original fibroblasts (Fibro). Samples are labeled as to the fibroblast of origin (see Table S1). hiN cell preparations clustered together, rather than with the originating fibroblast preparations.

(E and F) The five most significantly enriched gene ontology (GO) categories among the genes upregulated (E) or downregulated (F) in the context of hiN cell conversion are presented. Expression data were analyzed using a false discovery rate of less than 25% and a log-ratio threshold of > 2 . Nominal p values are listed.

(G) Heat map specifying the genes and expression values within the GO category "neuron projection" as in (E). Relative expression levels of individual genes (as labeled on rows) are presented from low (green) to high (red) as per the color chart bar at the bottom. Cell samples are labeled as per (D).

See also Figure S2, Figure S3, and Table S2.

Figures 3I and 3M–3O). In contrast to hiN cell reprogramming, differentiation of human iPS cells to a neural progenitor state led to the robust accumulation of Sox2-positive, Pax6-positive, and Nestin-positive progenitors, as expected (Figures 3D, 3H, and 3L). RNA expression profiling by real-time quantitative RT-PCR similarly indicated that expression of neuronal progenitor markers such as *FOXP1* and *OTX2* was absent from hiN cell cultures (Figure 3P).

Physiological Properties of hiN Cells

The majority of hiN cells displayed typical neuronal Na^+ , K^+ , and Ca^{2+} channel properties as assessed by patch-clamp recordings of cells at days 21–28 of culture. Specifically, TTX-sensitive Na^+ currents were characterized by a typical current density-voltage relationship (Figures 4A and 4B; confirmed in 18 of 22 cells

analyzed). Outward K^+ currents, inhibited in the presence of intracellular cesium (Cs^+), were readily apparent (Figures 4C and 4D; confirmed in 14 of 16 cells analyzed). Calcium channel function, measured using Barium (Ba^{2+}) as the charge carrier, displayed typical neuronal characteristics (Figure 4E; confirmed in 3 of 4 cells analyzed). Consistent with such channel properties, most hiN cells were able to fire at least one action potential in response to depolarizing current injections in current clamp mode (Figure 4F; 9 of 10 cells analyzed). Furthermore, upon termination of hyperpolarizing pulses, cells displayed a typical rebound spike (Figure 4F). Passive membrane properties were also consistent with an in vitro neuronal phenotype, with a resting membrane potentials ranging from -67 mV to -32 mV (average -52 mV; $n = 17$), membrane time constant (τ) ranging from 1.00 to 0.30 ms, membrane resistance (R_m) ranging from 0.12 to

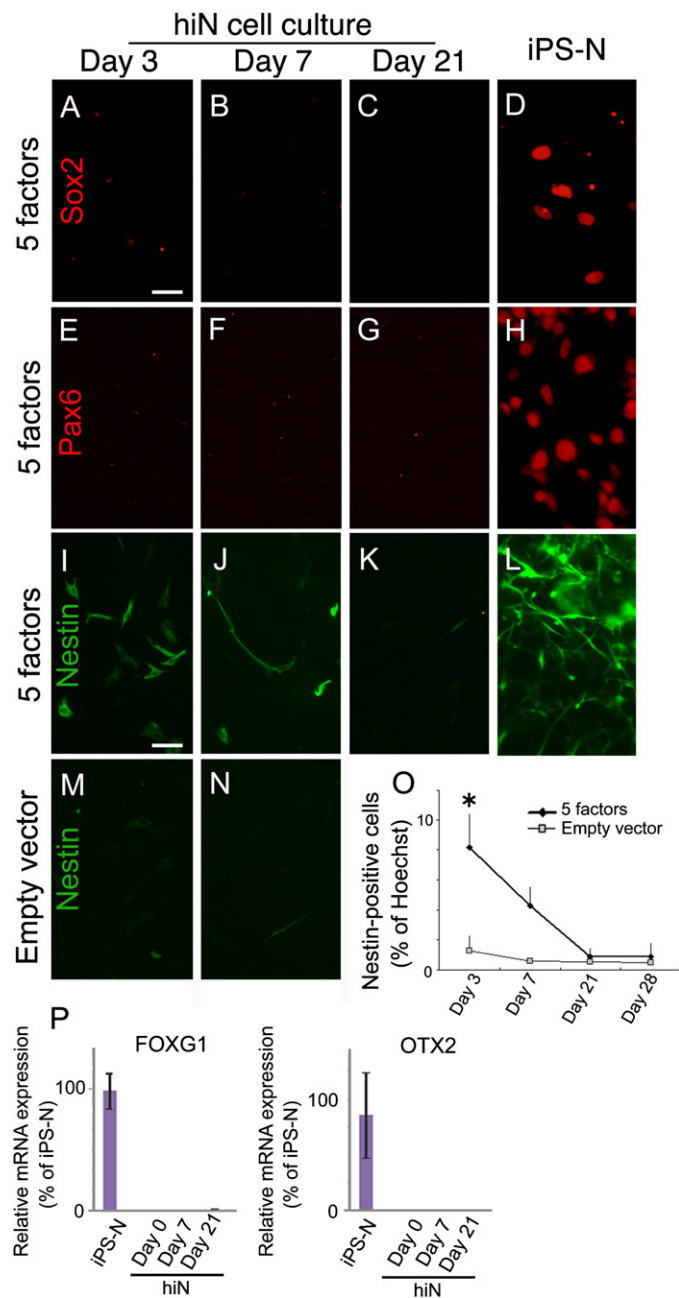


Figure 3. hiN Cell Reprogramming Is Directed

(A–H) Progenitor markers are not detected in hiN cell cultures. Sox2 (A–C) and Pax6 (E–G) expression were not detected during hiN cell reprogramming at 3, 7, and 21 days after transduction. In contrast, human iPSC cultures differentiated toward a neuroblast stage (iPS-N; D and H) displayed prominent intranuclear expression of the factors. Scale bar, 20 μ m. (I–N) Nestin is transiently expressed in a subset of cells within hiN cell cultures (I–K), albeit less robustly than in iPS-N cells (L). Staining was not apparent in empty vector-transduced cells (M and N). (O) Temporal profile of Nestin-positive cells in hiN cell cultures or empty vector-transduced skin fibroblasts. $n = 3$ at each time point. * $p < 0.05$ by ANOVA with Bonferroni correction. Results represent the mean \pm SEM. (P) Quantitative real-time RT-PCR analysis of neural progenitor marker gene expression in hiN cell cultures at 0, 7, or 21 days after transduction as indicated or in iPS-N cells. Expression levels are normalized to GAPDH; error bars represent the standard error of the mean (SEM); $n > 9$ per group.

larization-evoked fluorescence intensity changes were apparent within the axon-like processes of hiN cells (Figure 4K; seen in 6 of 10 cells), which are thought to represent putative synaptic release sites (Forti et al., 2000).

hiN Cells Can Integrate into Neuronal Circuitry In Vitro and In Vivo

We did not observe spontaneous activity that is suggestive of neuronal connectivity in hiN cells voltage clamped at -70 mV using the standard culture conditions as above ($n = 16$ of 16 cells tested). We therefore sought to develop alternative protocols that may provide the appropriate environmental cues for synaptic maturation. First, as glial cells can play a major role in the regulation of neuronal synaptic development and connectivity (Eroglu and Barres, 2010), hiN cells were cocultured with murine glial cells (obtained from mice ubiquitously expressing red fluorescent protein) (Muzumdar et al., 2007). After 2 weeks of coculture, whole-cell patch-clamp recordings of hiN cells (identified as nonfluorescent cells with a neuronal morphology) held at -70 mV revealed spontaneous membrane current changes that were sensitive to glutamatergic receptor inhibition with NBQX and APV (Figures 5A–5C; $n = 6$ of 10 cells tested).

Second, GFP-labeled hiN cells were transplanted in utero into embryonic day 13.5 mouse brain (Brüstle et al., 1997). The transplanted cells migrated from the ventricles into various brain regions, as expected (Figures 5D and 5E and Table S3). The identity of GFP-positive transplanted hiN cells was confirmed by immunostaining with an antibody specific for human NCAM (Figure 5F). Voltage-clamp recordings from GFP-positive hiN cells within acutely prepared brain slices from postnatal day 7 pups demonstrated spontaneous currents of various amplitudes and frequencies (Figure 5G; $n = 3$). These events increased in frequency and amplitude upon blockade of GABA_A receptors with picrotoxin (Figure 5H) and were suppressed with the glutamatergic receptor channel inhibitors NBQX and APV (Figure 5I). We confirmed the identity of the recorded cell by dual fluorescence imaging (Figures S4A and S4B). Subsequent to the recording, slices were immunostained to demonstrate expression of the human-specific mitochondrial marker hMito within recorded cells (Figure S4C; $n = 3$). Together,

1.7 G Ω , and capacitance ranging from 22 to 70 pF. We further evaluated γ -aminobutyric acid (GABA)-ergic and glutamatergic ligand-gated ion channel activity in hiN cells. hiN cells responded to exogenous puff application of glutamate or GABA, displaying typical depolarizing and hyperpolarizing currents, respectively (Figures 4G–4J; 7 of 7 cells analyzed). Finally, to provide functional evidence that hiN cells possess elements of the intrinsic machinery for synaptic vesicle release, we quantified local calcium transients within axon-like processes in the context of membrane step depolarization (using the fluorescent calcium indicator Oregon Green-BAPTA [OG-1]). Highly localized, depo-

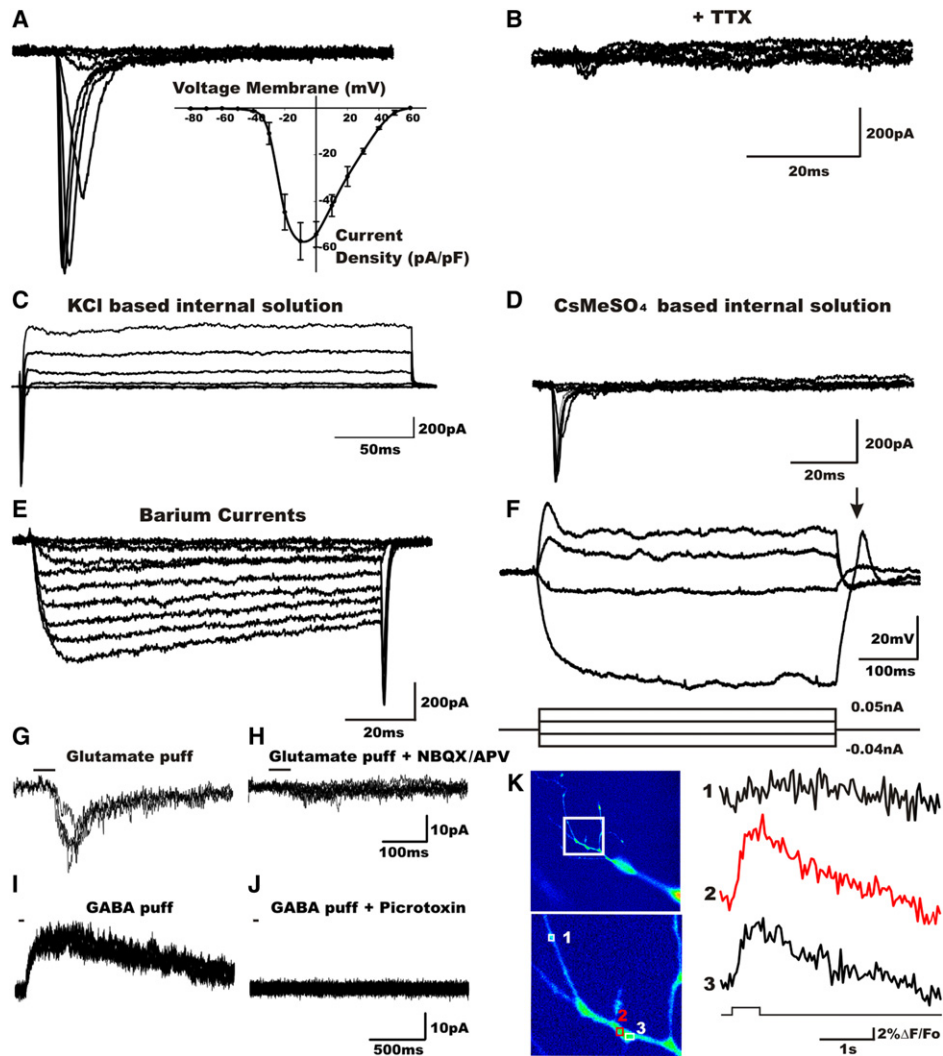


Figure 4. Electrophysiological Characterization and Evoked Calcium Transients of Cultured hiN Cells

(A) An example voltage-clamp recording from an hiN cell. Stepping the membrane voltage from -80 mV to more depolarized potentials (-70 to $+60$ mV in 10 mV increments) resulted in fast inward currents in 18 of 22 cell analyzed. Shown are example traces between -40 to 0 mV. Inset illustrates the pooled current density-voltage relationship (error bars represent the SEM).

(B) The fast inward currents were sensitive to bath application of the Na^+ channel blocker tetrodotoxin (TTX, 600 nM).

(C) Outward K^+ currents were obtained (in 14 of the 16 hiN cells recorded) with a KCl-based pipette solution upon depolarizing steps as described above.

(D) Minimal or no outward K^+ currents were observed in cells recorded with a Cs^+ -based pipette solution, as expected, but note the presence of the inward sodium currents.

(E) Macroscopic whole-cell voltage-dependent Ca^{2+} channel activity of hiN cells was identified using Ba^{2+} as the charge carrier. Currents were elicited in response to depolarizing steps from -70 mV in 10 mV steps (in 3 of the 4 hiN cells analyzed).

(F) In current-clamp mode, hiN cells exhibited a rebound action potential (arrow) at the end of hyperpolarizing current injections and action potentials upon depolarizing current injection. Bottom panel is a time schematic of the current injection protocol.

(G) Glutamate-mediated postsynaptic currents (PSCs) were elicited by focal application of 1 mM glutamate puffs for 50 ms in cells voltage clamped at -70 mV; shown are three traces elicited once every 3 min.

(H) Induced PSCs were sensitive to the AMPA channel blocker NBQX (20 μM) and the NMDA blocker APV (50 μM).

(I) Focal application of GABA (50 ms puff, 1 mM) to cells voltage clamped at $+20$ mV and dialyzed with a low Cl^- solution elicited current responses; shown are three traces evoked every 3 min.

(J) GABA-mediated currents were sensitive to the GABA_A antagonist picrotoxin (50 μM). Puff applications of neurotransmitter are indicated by a solid line above the tracings.

(K) (Upper-left) Fluorescence pseudocolor image of a complex axon-like process in an hiN cell dialyzed with 100 μM of the calcium indicator OG-1 (Oregon Green 488 BAPTA-1). (Lower-left) A higher-magnification view of a segment of this process (as demarked by white square in the top panel); individual regions of interest (ROIs) are indicated by numbered squares within the bottom panel. (Right) Time courses of the relative change in fluorescence ($\Delta F/F_0$) in individual ROIs, as numbered in the lower-right panel. Calcium transients were evoked by 200 ms depolarizing pulses ($V_h = -70$ to 0 mV) in the soma. ROIs #2 and #3 display calcium transients (hot spots), but no response was elicited in ROI #1.

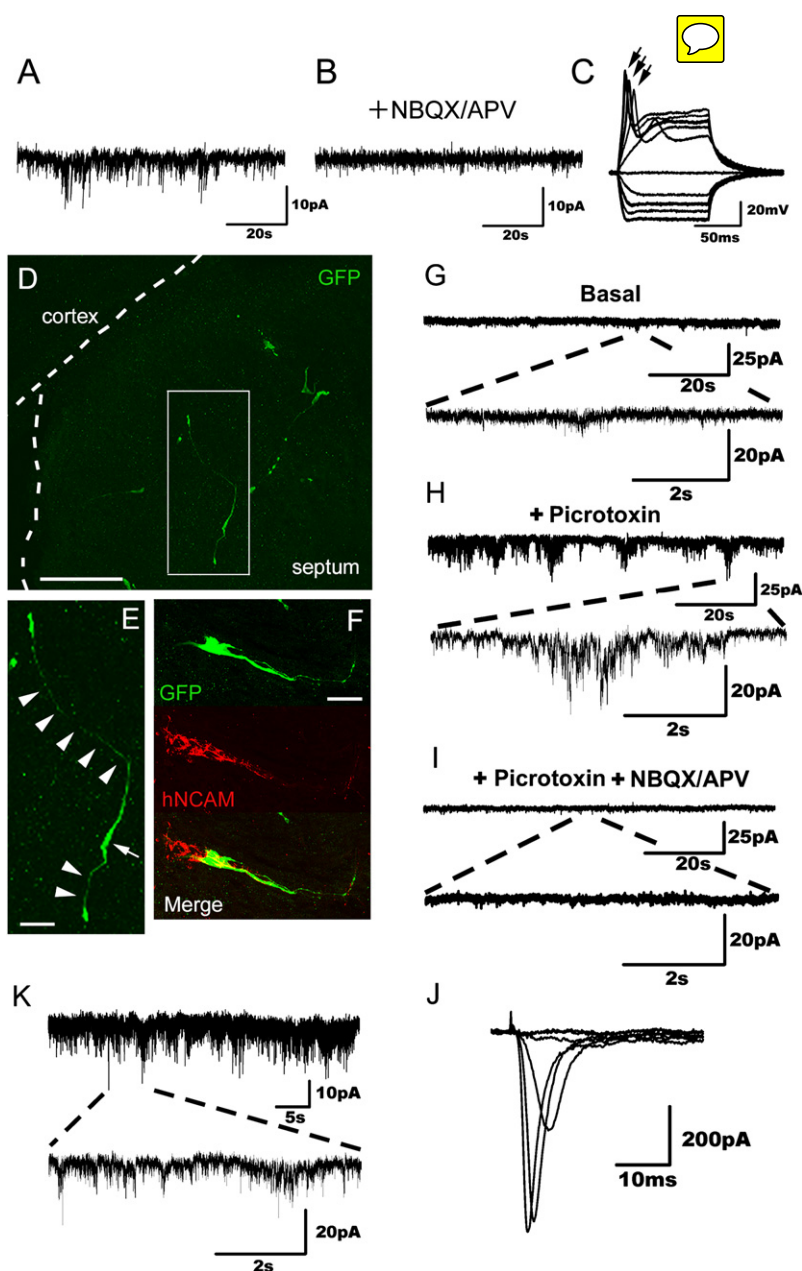


Figure 5. Evidence of hiN Cell Functional Integration

(A) Representative spontaneous postsynaptic currents recorded from an hiN cell present in a murine glial monolayer coculture. The cell was held at -70 mV. Events of various amplitudes (5–20 pA) are seen.

(B) Spontaneous postsynaptic currents as observed in (A) were abolished by bath application of NBQX/APV.

(C) Upon depolarizing current injections in current-clamp mode, action potentials were induced. Individual traces represent independent recorded events; action potentials (indicated by arrows) were seen in five of the nine tracings. (D and E) Confocal fluorescent images of brain slices prepared from postnatal day 3 animals that had been grafted in utero with hiN cells. Transplanted hiN cells migrated extensively and extended neurite processes. An arrowhead indicates cell soma; arrows point to apparent processes. Scale bars: (D) 100 μ m, (E) 20 μ m.

(F) Confocal reconstruction of a transplanted GFP-positive hiN cell stained with a human-specific NCAM antibody. GFP, green; hNCAM, red. Scale bar, 50 μ m.

(G) Voltage-clamp recording of an hiN cell ($V_h = -70$ mV) integrated into the piriform cortex of the host brain, demonstrating spontaneous events of low frequency and amplitude.

(H) The frequency and amplitude of the spontaneous excitatory postsynaptic currents (sEPSCs, as in G) increased upon blockade of GABA_A receptors with 50 μ M picrotoxin.

(I) sEPSCs were drastically reduced by blocking glutamatergic synaptic transmission with 20 μ M NBQX and 50 μ M APV.

(J) Sodium currents of the same cell (G–I) elicited by voltage steps from $V_h = -70$ mV (-60 to -20 in 10 mV steps).

(K) Representative voltage-clamp recording at a holding potential ($V_h = -70$ mV) of an hiN cell integrated into the cingulate gyrus of the host brain. Traces show spontaneous slow and fast currents of different amplitudes, indicating that this neuron receives synaptic contacts from host cells.

See also Figure S4 and Table S3.

these findings support the idea that hiN cells are capable of neuronal connectivity.

Generation of hiN Cells from FAD and SAD Patient Skin Fibroblasts

As proof of principle for their utility in disease modeling, we generated hiN cells from a panel of human skin fibroblasts derived from patients with familial AD (FAD) due to mutations in PSEN-1 or -2, patients with sporadic AD (SAD), or unaffected individuals (UND; $n = 3$ per each group). Given the likely heterogeneity of “sporadic” disease and the limited number of samples examined in our study, we subsequently focused herein on phenotypic examination of the familial lines. hiN cells derived from disease-

associated fibroblasts appeared similar to those from unaffected individuals with respect to neuronal reprogramming characteristics, such as efficiency of MAP2-positive hiN cell generation and the percentage of neurons that express vGLUT1 (Figures 1O and 1P). Induction of expression of the mature neuron marker synaptophysin was comparable among the hiN cell cultures, as determined by quantitative real time RT-PCR analysis (Figure S5A), and cell density at 3 weeks was not significantly different across the hiN cell cultures (Figure S5B).

APP Processing in FAD- and SAD-Derived hiN Cells

We next evaluated AD-associated phenotypes in the hiN cell cultures, including the processing of amyloid precursor protein (APP) to the A β 42 and A β 40 fragments. FAD patient brain is typified by an increased A β 42/A β 40 ratio (Hardy and Selkoe, 2002). Consistent with this, the A β 42/A β 40 ratio was dramatically increased in FAD hiN cell cultures relative to UND hiN cell

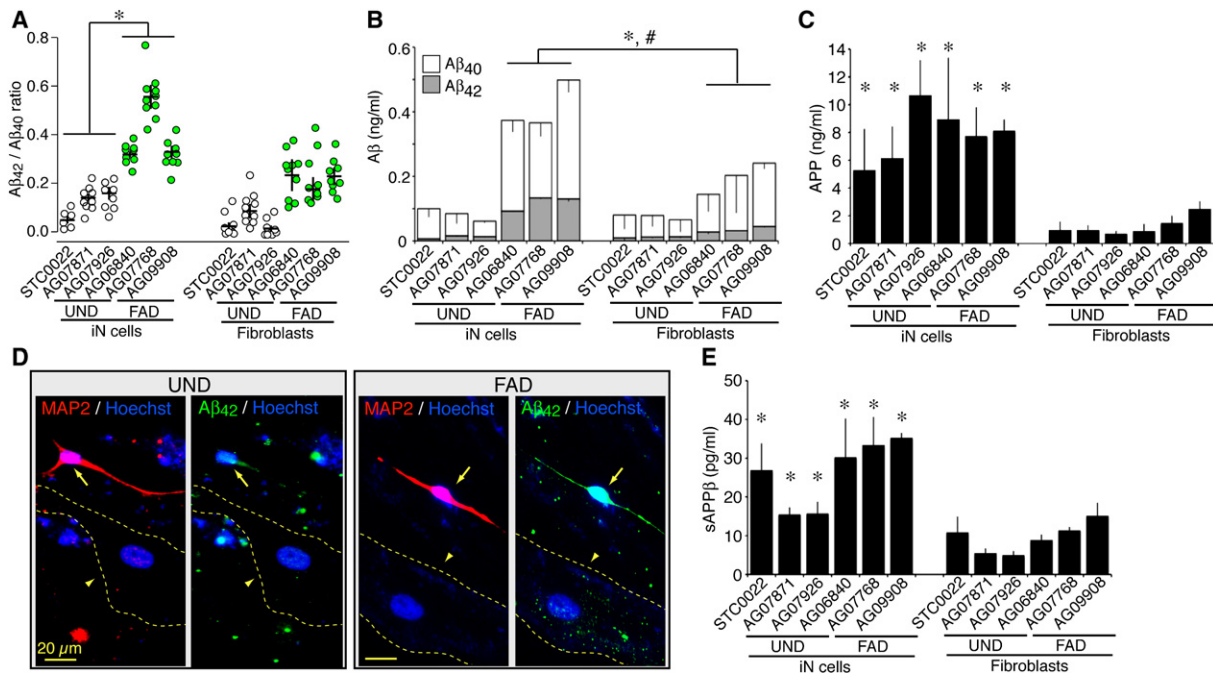


Figure 6. Modified APP Processing in FAD hiN Cell Cultures

(A) The A β 42/A β 40 ratio is selectively increased in FAD hiN cell cultures relative to UND hiN cell cultures or fibroblasts. Media from hiN cell cultures (at 3 weeks posttransduction, empty circles) or fibroblast cultures (green circles), as indicated, was assayed for secreted A β 40 and A β 42 by sandwich ELISA. Results represent the mean \pm SEM. $n = 3$ individual lines per group, with 11 to 16 independent wells for each line. * $p < 0.05$ by ANOVA with post hoc Tukey HSD test.

(B) Total absolute extracellular A β levels (A β 40 [white bars] + A β 42 [gray bars]) are presented for cultures as in (A). Total A β was increased by neuronal hiN cell conversion in the context of FAD patient cultures. In contrast, UND fibroblast cultures were not significantly different from UND hiN cell cultures. $n = 3$ individual lines per group, with 11 to 16 independent wells for each line. * $p < 0.05$. Results represent the mean \pm SEM.

(C) Quantification of total intracellular APP holoprotein using sandwich ELISA. APP is enriched in hiN cell cultures relative to fibroblast precursors (* $p < 0.05$ for all comparisons.), but UND and FAD genotypes do not differ significantly. Results represent the means \pm SEM ($n = 6-9$ wells per group). * $p < 0.05$.

(D) MAP2-positive neuronal cells within the hiN cultures are enriched for the A β 42 fragment, compared to fibroblastic MAP2-negative cells. FAD and UND hiN cell cultures were immunostained with antibodies to MAP2 (left, red) along with A β 42 (right, green); nuclei are identified by Hoechst staining (blue). MAP2-negative fibroblastic cells (demarcated with dotted lines) display low levels of A β 42 relative to the MAP2-positive cells, as quantified in Figure S5J.

(E) Accumulation of sAPP β in the media of UND and FAD cultures, as determined by sandwich ELISA. Results represent the means \pm SEM; $n = 4-5$ wells per individual line.

See also Figure S5.

cultures, as quantified in cell media by ELISA (Figure 6A; $p < 0.001$, ANOVA with post hoc Tukey HSD; $n = 3$ patient lines per FAD or UND group with 11–16 independent cultures per line). Similarly, on a pooled analysis of all FAD hiN versus all UND hiN cultures, the A β 42/A β 40 ratio is significantly increased in the FAD group ($p < 1 \times 10^{-9}$; ANOVA with post hoc Tukey HSD; $n > 38$ per group). The increased A β 42/A β 40 ratio is most evident in the AG07768 line, but even in the absence of those AG07768 samples, the FAD group displayed an elevated A β 42/A β 40 ratio ($p < 1 \times 10^{-9}$; ANOVA with post hoc Tukey HSD, $n > 29$ per group). Importantly, the A β 42/A β 40 ratio in FAD hiN cell cultures was also elevated relative to the originating FAD fibroblast cultures ($p < 1 \times 10^{-9}$; ANOVA with post hoc Tukey HSD; $n > 38$ per group). In contrast, the A β 42/A β 40 ratio in UND hiN cell cultures was not significantly elevated relative to the originating UND fibroblast cultures ($p > 0.05$; ANOVA with post hoc Tukey HSD; $n > 30$ per group). FAD hiN cell conversion led to an increase in the level of total A β (combined A β 42 and A β 40 polypeptides) relative to the originating FAD fibroblasts (Figure 6B; $p < 0.05$; ANOVA with post hoc Tukey HSD; $n = 3$ individual lines per group,

with 11 to 16 independent wells for each line). Such an increase in total A β with hiN cell conversion was not apparent in the context of UND cultures. Taken together, these data indicate that hiN cell conversion appears to amplify an FAD-associated phenotype in the context of PSEN1 or PSEN2 mutations.

Levels of APP holoprotein (the A β 42 and A β 40 precursor) did not differ significantly between hiN cell cultures from FAD patients versus UND controls, as quantified by ELISA on cellular lysates (Figure 6C) or by quantitative real-time RT-PCR on RNA transcripts (Figure S5C). However, in comparison to the original fibroblast cultures, holoprotein expression was consistently elevated with all hiN cell cultures regardless of origin (Figure 6C). Because hiN cultures from FAD and UND genotypes displayed similar levels of APP, it is unlikely that APP levels account for the selective generation of A β 42 in FAD hiN cells. Using coimmunostaining with antibodies to A β 42, A β 40, and MAP2, we further observed that both isoforms of A β are selectively increased in the MAP2-positive neuronal cells, but not in the remaining fibroblastic cells, that compose the mixed hiN culture (Figures 6D and Figures S5H–S5J).

Cleavage of APP by BACE1 β -secretase activity is thought to be a rate-limiting step in the production of A β and precedes cleavage by γ -secretase (Thinakaran and Koo, 2008). We thus quantified the soluble extracellular cleavage product of APP by BACE1, termed sAPP β , in the hiN cell cultures. There was a consistent increase in the sAPP β product in converted FAD and UND hiN cell cultures relative to their respective fibroblasts. However, accumulation of sAPP β was not significantly elevated in hiN cell cultures from FAD patients relative to hiN cell cultures from UND individuals (Figure 6E). BACE1 transcript levels, as determined by quantitative real-time RT-PCR, did not appear altered in hiN cell cultures relative to fibroblasts, regardless of disease status (Figure S5D). Thus, the elevated level of A β 42 in hiN-FAD is not caused by increased activity of BACE1.

Altered APP-Positive Endocytic Compartment Morphology in FAD hiN Cells

Immunocytochemical analysis of hiN cells with an antibody to the APP amino terminus domain revealed the presence of APP-positive puncta within soma (Figures 7A and 7B). In contrast, such APP-positive punctate structures were not readily apparent in the originating fibroblasts. Quantitative analysis of APP staining of hiN cells revealed that APP-positive puncta (defined as 0.1 to 1 μ m in diameter) are significantly increased in FAD-derived hiN cell cultures, relative to UND hiN cells, quantified in terms of total puncta area per cell (Figure 7C; FAD, $78.2 \pm 10.93 \mu\text{m}^2$; UND, $23.8 \pm 3.28 \mu\text{m}^2$). This is due to an increased number of puncta per cell as well as an increased average size of puncta (Figures S6A and S6B). Similar findings were apparent with a second independent antibody to APP (Figure S6I). Pathological studies of sporadic AD patients at autopsy have reported evidence for alteration in the size of intracellular vesicular endocytic (Cataldo et al., 1997) and lysosomal (Cataldo et al., 1996) compartments.

APP processing by the β - and γ -secretase activities may largely proceed within vesicular endosomal compartments (Tang, 2009). We thus further characterized the APP-positive punctate structures in hiN cells by costaining with antibodies for a panel of vesicular compartment and plasma membrane markers. Subpopulations of APP-positive puncta in hiN cells stained positively for an early endosomal marker, early endosome-associated antigen-1 (EEA1); a late endosomal marker, the cation-independent mannose 6-phosphate receptor (MPR); and a lysosomal marker, the lysosomal associated marker protein-2 (LAMP2). Localization to the plasma membrane at the cell periphery was also observed (quantified in terms of colocalization at a membrane dye, CellMask). Of these populations, the EEA1-positive, APP-positive compartment was significantly increased in FAD hiN cells relative to UND cells, as quantified by the percentage of APP-positive puncta stained with EEA1 (Figures 7D–7F; FAD, $24\% \pm 2\%$; UND, $13\% \pm 1\%$). In contrast, APP puncta staining at the plasma membrane appeared significantly reduced in the FAD hiN cells (FAD-hiN, $2.1\% \pm 1.3\%$; UND-hiN, $6.3\% \pm 1.0\%$; Figures 7G–7I). APP-positive endocytic puncta also stained for BACE1 (Figure 7J–7L and Figure S6I; FAD, $54.2 \pm 2.91 \mu\text{m}^2$; UND, $16.5 \pm 0.83 \mu\text{m}^2$), as expected given the known localization of BACE1 (Vassar et al., 1999). Finally, we note that EEA1-positive and

MPR-positive puncta were generally enlarged in FAD cells (Figures 7D–7F and Figures S6C–S6E), regardless of costaining with APP, indicative of a broadly altered endocytic compartment, rather than a specific defect in APP-positive structures.

We next sought to clarify whether altered APP-positive puncta morphology in FAD-derived hiN cells might simply be a secondary consequence of A β accumulation. Treatment with a γ -secretase inhibitor, DAPT, which suppressed production of A β (Figures S6K and S6L), did not prevent increased APP-positive puncta area per cell in the context of the FAD lines (Figures 7M–7O). Rather, we found that DAPT treatment of UND hiN cells, but not FAD hiN cells, partially phenocopied the magnified APP-positive intracellular compartment (Figures 7M–7O). Thus, the increased APP-positive puncta seen with DAPT of UND hiN cells was occluded in the context of FAD hiN cell cultures (that already harbor increased total APP-positive puncta).

Finally, to relate the altered intracellular APP-positive puncta in FAD hiN cells to FAD mutations, we performed a “rescue” experiment by overexpressing wild-type PSEN1 into FAD PSEN1 mutant hiN cells. Although FAD mutations are dominantly inherited in human patients, it is well described that overexpression of PSENs leads to preferential replacement of the endogenously encoded form by the exogenous overexpressed gene product (in part, a consequence of reduced stability of the endogenously encoded gene product; Thinakaran et al., 1997). Consistent with this, we found that overexpression of wild-type PSEN1 by transfection of a plasmid vector into hiN cell cultures rescued the endosomal APP-positive endocytic phenotype; transfection of this vector into UND cells did not appear to alter intracellular APP-positive puncta staining (Figures 7P–7R). These findings suggest that the FAD phenotype is caused, at least in part, by abnormal endocytic function, which is dependent on PSEN.

DISCUSSION

A major goal in regenerative medicine is the facile generation of human neurons for cell replacement therapeutics or disease modeling. The description of hiPS cell reprogramming methods for the generation of pluripotent cells has fueled excitement in the field. But as hiPS cell generation is complex, time-consuming, and associated with tumorigenicity and genomic DNA rearrangements (Pera, 2011), alternative approaches are of interest. By comparison to hiPS cell reprogramming, hiN cell conversion offers a more directed route to terminally differentiated neurons.

Our analysis of FAD patient-derived hiN cell cultures underscores the potential utility of such human neuronal disease models. hiN cells from PSEN mutant FAD patient fibroblasts display an increased A β 42/A β 40 ratio relative to UND hiN cells, consistent with patient brain pathology and with the well-characterized role of PSENs as essential components of the γ -secretase complex (Hardy and Selkoe, 2002). Surprisingly, the impact of FAD PSEN mutations on the A β 42/A β 40 ratio was amplified upon hiN cell conversion from fibroblasts. This suggests a model in which PSEN FAD mutants may alter APP processing at multiple levels: directly through modified γ -secretase activity, as well as indirectly with altered cellular context. Consistent

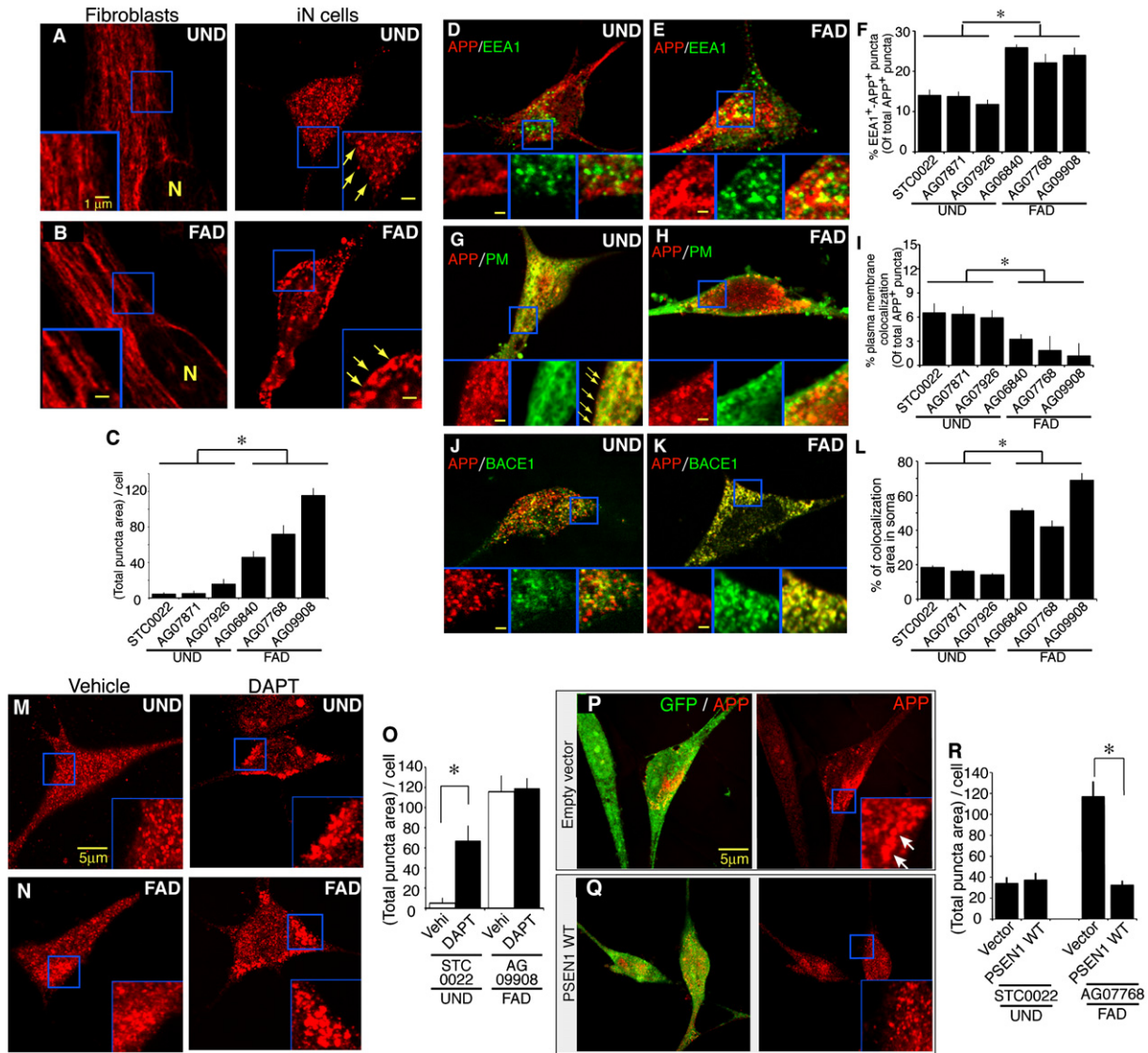


Figure 7. APP Is Enriched within Modified Endocytic Compartment Puncta in FAD hiN Cells

(A and B) APP immunostaining of hiN cells (right) derived from representative UND (A, AG07926) and FAD (B, AG09908) cultures labels punctate structures that are typical of endocytic compartment vesicles. In contrast, control fibroblast cultures display a distinct labeling pattern, with sparse punctate morphology (left). Insets show high-magnification views for visualization of APP-positive puncta (arrows). N, nuclei.

(C) Quantification of APP-positive total puncta area per cell (μm^2 , number of puncta per cell \times average puncta area) in individual UND and FAD hiN cell cultures as labeled. Total APP-positive puncta area was significantly increased in FAD hiN cultures, relative to UND cultures, as a consequence of increased puncta size and number. Results represent mean \pm SEM ($n = 12\text{--}38$ cells in a total of 6 wells per group). $^*p < 0.05$.

(D–F) Colocalization of APP-positive puncta with the early endosomal marker EEA1 in UND and FAD hiN cells. APP-positive puncta (in red) appeared partially colocalized with EEA1 (in green), and this was most prominent in FAD (E) relative to UND (D) cultures. Colocalization was visualized as yellow in the merged images. Inset panels present merged as well as individual staining patterns for visualization of areas, as demarcated by a blue square. (F) Quantification of APP and EEA1 colocalization by fluorescent microscopy as in (E). Puncta are defined here as distinct signal intensities 0.1–1 μm in diameter using Image J analysis software (NIH).

(G–I) A subset of APP-positive puncta is costained with a plasma membrane marker at the cell periphery (PM, in green). In contrast to EEA1 costaining, peripheral plasma membrane marker costaining appears reduced in the FAD hiN cells (H) relative to UND hiN cells (G). Insets are high-magnification views of areas demarcated by blue squares. Arrows point to examples of APP puncta at cell cortex. Quantification of colocalization by fluorescent microscopy is shown in (I). (J–L) Double immunostaining of hiN cells for APP and BACE1. Colocalization of APP and BACE1 was assessed in UND (J) and FAD (K) hiN cells. Quantification of the data shows increased colocalization in the FAD cultures, consistent with the preferential localization to intracellular endocytic vesicles (L). All results represent the means \pm SEM ($n = 35\text{--}48$ cells in 3–6 independent wells per group). $^*p < 0.05$.

(M–O) Enlarged APP-positive puncta in UND hiN cells treated with the γ -secretase inhibitor DAPT. UND (M, AG07926) and FAD (N, AG09908) hiN cells were treated with either vehicle (left) or DAPT (right) for 18 hr and then fixed and stained with an antibody to the APP amino terminus. Insets at lower right show high-magnification views for visualization of enlarged APP-positive puncta. (O) Quantification revealed that γ -secretase inhibitor treatment led to a significant

with this model, we show that intracellular localization of APP within vesicular endocytic structures is modified in the context FAD PSEN hiN cells.

Prior pathological autopsy studies of early-stage AD patient brain have reported the presence of altered endosomal, lysosomal, and autophagy compartments (Nixon and Cataldo, 2006). Furthermore, a complete deficiency of PSEN-1 and -2 in fibroblasts can impair endosomal trafficking (Repetto et al., 2007). However, the impact of FAD PSEN mutations on neuronal APP-positive endosomal structures has not previously been characterized. Our analysis further indicates that γ -secretase inhibition in UND hiN cell cultures appears to mimic the APP-positive endosomal compartment phenotype of FAD cultures, suggesting a role for reduced γ -secretase activity in this FAD phenotype. It remains possible that FAD-associated endosomal compartment modifications, as observed in FAD hiN cells, play a pathogenic role in AD independent of A β . The issue is complicated by the many functionally heterogeneous FAD-associated PSEN1 and PSEN2 mutations. An important limitation to our present study is that we evaluate only two such forms, and thus future studies with additional lines would likely be informative.

Examination of FAD hiN cell models for additional AD-associated pathological findings, such as defective synaptic function, will be of interest. **To this end, the ability of hiN cells to functionally integrate into neuronal circuitry will be particularly useful. It is also conceivable that such integration of hiN cells into murine AD disease models will test the therapeutic potential of hiN cells.** Finally, we note that, in the future, it may well be feasible to evaluate mechanisms of sporadic AD pathology using hiN cell models.

EXPERIMENTAL PROCEDURES

Human Skin Fibroblasts

Human skin fibroblast cultures from nine individuals were used in this study (see Table S1). All lines were derived from de-identified, banked tissue samples. Human skin fibroblasts were cultured in standard fibroblast media (see Extended Experimental Procedures).

Plasmid Construction and Lentiviral Production

cDNAs for the reprogramming factors were cloned into lentiviral vectors either individually or as a polycistronic set (for *Ascl1*, *Brn2*, and *Zic1*; see Extended Experimental Procedures for cloning details). Production of replication-incompetent lentiviral particles was as described (MacLeod et al., 2006). Human wild-type *PSEN1* cDNA (Openbiosystems) was cloned into the pLenti6.3/V5-Dest vector using the Gateway LR cloning system (Invitrogen).

hiN Cell Induction and Transfection

Fibroblasts were transduced with replication-incompetent, VSVg-coated lentiviral particles encoding *Ascl1*, *Brn2*, *Myt11*, *Oligo2*, and *Zic1* at a multiplicity of infection of 2:1 and were maintained in fibroblast media for 2 days (see Extended Experimental Procedures). Subsequently, the media was replaced

with glial-conditioned N2 media (GCM; DMEM/F12 with N2 supplement; Invitrogen) containing 20 ng/ml BDNF and 20 ng/ml NT3 (Peprotech). For the first 4 days in GCM, dorsomorphin (1 μ M; Stemgent) was also supplemented. Media was changed every 2–3 days for the duration of the culture period. For the PSEN1 rescue study, cells were transfected with pLenti6.3/V5-Presenilin1 and pEGFP-C1 plasmids (9:1) using the Lipofectamine 2000 reagent (DNA: LF2000 1 μ g; 5 μ l in each well of 24 well, Invitrogen).

Immunocytochemistry, Immunohistochemistry, and RT-PCR

Immunocytochemistry and immunohistochemistry (IHC) were performed as previously described (MacLeod et al., 2006). Detailed antibody sources and dilutions utilized can be found in the Extended Experimental Procedures. Imaging was conducted by laser scanning confocal microscopy with a 63 \times /1.4 objective (LSM510, Carl Zeiss) or epifluorescence microscope (Olympus 1X71; Japan). Cell counts and fluorescence intensities were quantified within 10–35 images of randomly selected views per well. Subsequently, images were analyzed for cell counts and fluorescent intensity using Image J 1.42q software (National Institute of Health, USA). Values are presented as mean \pm SEM. Quantitative real time RT-PCR was performed as described (Rhinn et al., 2008); primer pairs utilized are detailed in the Extended Experimental Procedures. Gene expression levels were quantified by the $\Delta\Delta$ Ct method (Rhinn et al., 2008).

FACS and Transcriptome Analyses

hiN cells (10⁶ cells) were stained with an antibody to NCAM (BD Bioscience) and then sorted on a FACS Aria Ilu (BD Bioscience, CA) directly into RNA lysis solution (Ambion, TX). RNA was extracted from cell preparations using the RNAqueous Micro Kit (Ambion). Concentration and quality of RNA were assessed using the Bioanalyzer system (Agilent). mRNA was amplified and labeled using Ovation Pico WTA System (Nugen) and was subsequently hybridized to Human Genome U133 Plus 2.0 Arrays (Affymetrix). Raw data were processed using the R statistical computing environment Affymetrix Linear Modeling Graphical User Interface package (affylmGUI). Computational methods are detailed in the Extended Experimental Procedures.

In Utero Transplantation

Human skin fibroblasts (STC0022) were labeled by transduction with a GFP-encoding lentiviral vector and then passaged three times over 10 days prior to initiation of hiN cell induction to remove residual lentivirus. hiN induction was then performed using the lentiviral vectors encoding *Ascl1*, *Brn2*, *Myt11*, *Oligo2*, and *Zic1*, as described above. At 7–10 days later, cells were trypsinized and triturated to single-cell suspensions in the presence of 0.1% DNase (QIAGEN). Timed pregnant C57BL/6N mice at day 13.5 of gestation were anesthetized with oxygen containing 2% isoflurane administered through an inhalation mask, and 2–5 \times 10⁵ cells were injected into the telencephalic vesicle of each embryo as described (Brüstle et al., 1997). Transplanted mice were spontaneously delivered and analyzed at the time points indicated. Following deep isoflurane anesthesia, mice were euthanized, and the brains were rapidly removed and fixed in 4% paraformaldehyde for 2 days. For IHC, 50 μ m sections were cut with a vibrating blade microtome.

Electrophysiology and Calcium Imaging

Tight-seal whole-cell recordings (WCR) were performed with borosilicate glass pipettes (resistance 5–8 M Ω) using an Axopatch 200B amplifier (Axon Instruments). Recordings from transplanted cells were performed in acutely prepared brain slices (180 μ m thick) through the entire cerebrum, as described in detail (Llano and Bezanilla, 1980). For glial coculture studies, murine astroglial cells were prepared as previously described (Kaech and Banker, 2006)

increase in total APP-positive puncta area per cell within UND, but not FAD, cultures. Results represent mean \pm SEM (n = 35–50 cells in 3 independent wells). *p < 0.05.

(P–R) Rescue of the endosomal APP-positive endocytic phenotype in PSEN1 mutant FAD hiN cells. UND (P, STC0022) and PSEN1 mutant FAD (Q, AG07768) hiN cell cultures were transfected with an expression vector for human wild-type PSEN1 or empty vector (along with EGFP to mark transfected cells). Cultures were incubated for an additional 72 hr and subsequently immunostained for APP. Results represent the mean \pm SEM (n = 35–50 cells in 3 independent wells per group).

*p < 0.05.

See also Figure S6.

from mice ubiquitously expressing red fluorescent protein (Muzumdar et al., 2007). For calcium imaging, Oregon Green-BAPTA 1 (OG1; Molecular Probes) was added at a concentration of 100 μ M. Fluorescent imaging was conducted using a digital EM-CCD camera (Andor ixon) with an LED light source (Cairn). Values are expressed as the percentage of change in fluorescence signal with respect to prestimulus control, $\Delta F/F_0 = 100 \times (F - F_0)/(F_0 - B)$, wherein F is the fluorescence at any given time, F_0 the average at the prestimulus period, and B the average value of the background fluorescence at each time point, as quantified in four regions of the imaged field that do not contain any part of the dye-filled cell.

Sandwich ELISAs

APP ELISA was performed using a human APP ELISA kit (Invitrogen, Camarillo, CA), according to the manufacturer's instruction. Absorbance was read on a VersaMax ELISA Microplate Reader (Molecular Devices, Inc., Sunnyvale, CA) at 450 nm. The amount of APP was normalized to the total cell protein (determined with the DC Protein Assay Reagent kit; Bio-Rad, Hercules, CA). sAPP β ELISA was performed using BetaMark sAPP Beta ELISA kit (Covance, Princeton, NJ), according to the manufacturer's instruction. The chemiluminescence was read on a microplate luminometer (SPECTRAFluoR Plus, TECAN, Männedorf, Switzerland). A β quantification was performed by ELISA as described previously (Cirrito et al., 2003).

Statistical Analysis

Statistic analyses were performed with the Ystat 2002 software (Igakyo Tosho Shuppan Co., Ltd., Tokyo, Japan) together with Microsoft Excel software (Microsoft Corp., Redmond, WA, USA) or by using R aov and TukeyHSD functions. The statistical significance of comparisons was assessed either by ANOVA with post hoc Tukey HSD (where indicated) or by nonparametric ANOVA Kruskal-Wallis H test, followed by post hoc Mann-Whitney U test with Bonferroni correction.

SUPPLEMENTAL INFORMATION

Supplemental Information includes Extended Experimental Procedures, six figures, and four tables and can be found with this article online at doi:10.1016/j.cell.2011.07.007.

ACKNOWLEDGMENTS

We are grateful to David Holtzman and John Cirrito for generously providing reagents for ELISA and Laura Baur for assistance with plasmid construction. We thank Arnon Rosenthal, Scott Small, and Oliver Hobert for reviewing the manuscript. Peter Koppensteiner, Laura Baur, and Ottavio Arancio helped in early stages of the project. We thank Mikako Sakurai for technical advice on in utero transplantation and the New York Stem Cell Foundation for FACS facility services. This work was funded, in part, by the Helmsley Foundation, New York State Stem Cell Science NYSTEM grants C024402 and C024403, and an anonymous foundation grant to A.A., as well as NIH grant AG027476 to H.M..

Received: December 9, 2010

Revised: June 1, 2011

Accepted: July 8, 2011

Published: August 4, 2011

REFERENCES

Abeliovich, A., and Doege, C.A. (2009). Reprogramming therapeutics: iPS cell prospects for neurodegenerative disease. *Neuron* 61, 337–339.

Alzheimer, A. (1907). Über eine eigenartige Erkrankung der Hirnrinde. *Allg Z Psychiat Psych-Gerichtl Med* 64, 146–148.

Bentahir, M., Nyabi, O., Verhamme, J., Tolia, A., Horr , K., Wiltfang, J., Esselmann, H., and De Strooper, B. (2006). Presenilin clinical mutations can affect gamma-secretase activity by different mechanisms. *J. Neurochem.* 96, 732–742.

Br stle, O., Spiro, A.C., Karram, K., Choudhary, K., Okabe, S., and McKay, R.D. (1997). In vitro-generated neural precursors participate in mammalian brain development. *Proc. Natl. Acad. Sci. USA* 94, 14809–14814.

Cataldo, A.M., Barnett, J.L., Pieroni, C., and Nixon, R.A. (1997). Increased neuronal endocytosis and protease delivery to early endosomes in sporadic Alzheimer's disease: neuropathologic evidence for a mechanism of increased beta-amyloidogenesis. *J. Neurosci.* 17, 6142–6151.

Cataldo, A.M., Hamilton, D.J., Barnett, J.L., Paskevich, P.A., and Nixon, R.A. (1996). Properties of the endosomal-lysosomal system in the human central nervous system: disturbances mark most neurons in populations at risk to degenerate in Alzheimer's disease. *J. Neurosci.* 16, 186–199.

Cirrito, J.R., May, P.C., O'Dell, M.A., Taylor, J.W., Parsadanian, M., Cramer, J.W., Audia, J.E., Nissen, J.S., Bales, K.R., Paul, S.M., et al. (2003). In vivo assessment of brain interstitial fluid with microdialysis reveals plaque-associated changes in amyloid-beta metabolism and half-life. *J. Neurosci.* 23, 8844–8853.

Davis, R.L., Weintraub, H., and Lassar, A.B. (1987). Expression of a single transfected cDNA converts fibroblasts to myoblasts. *Cell* 51, 987–1000.

De Strooper, B., and Annaert, W. (2010). Novel research horizons for presenilins and γ -secretases in cell biology and disease. *Annu. Rev. Cell Dev. Biol.* 26, 235–260.

Eroglu, C., and Barres, B.A. (2010). Regulation of synaptic connectivity by glia. *Nature* 468, 223–231.

Forti, L., Pouzat, C., and Llano, I. (2000). Action potential-evoked Ca²⁺ signals and calcium channels in axons of developing rat cerebellar interneurons. *J. Physiol.* 527, 33–48.

Gilyarov, A.V. (2008). Nestin in central nervous system cells. *Neurosci. Behav. Physiol.* 38, 165–169.

Hardy, J., and Selkoe, D.J. (2002). The amyloid hypothesis of Alzheimer's disease: progress and problems on the road to therapeutics. *Science* 297, 353–356.

Llano, I., and Bezanilla, F. (1980). Current recorded from a cut-open giant axon under voltage clamp. *Proc. Natl. Acad. Sci. USA* 77, 7484–7486.

MacLeod, D., Dowman, J., Hammond, R., Leete, T., Inoue, K., and Abeliovich, A. (2006). The familial Parkinsonism gene LRRK2 regulates neurite process morphology. *Neuron* 52, 587–593.

Muzumdar, M.D., Tasic, B., Miyamichi, K., Li, L., and Luo, L. (2007). A global double-fluorescent Cre reporter mouse. *Genesis* 45, 593–605.

Nixon, R.A., and Cataldo, A.M. (2006). Lysosomal system pathways: genes to neurodegeneration in Alzheimer's disease. *J. Alzheimers Dis.* 9(3, Suppl), 277–289.

Pera, M.F. (2011). Stem cells: The dark side of induced pluripotency. *Nature* 471, 46–47.

Repetto, E., Yoon, I.S., Zheng, H., and Kang, D.E. (2007). Presenilin 1 regulates epidermal growth factor receptor turnover and signaling in the endosomal-lysosomal pathway. *J. Biol. Chem.* 282, 31504–31516.

Rhinn, H., Marchand-Leroux, C., Croci, N., Plotkine, M., Scherman, D., and Escriou, V. (2008). Housekeeping while brain's storming Validation of normalizing factors for gene expression studies in a murine model of traumatic brain injury. *BMC Mol. Biol.* 9, 62.

Shen, J., and Kelleher, R.J., III. (2007). The presenilin hypothesis of Alzheimer's disease: evidence for a loss-of-function pathogenic mechanism. *Proc. Natl. Acad. Sci. USA* 104, 403–409.

Takahashi, K., and Yamanaka, S. (2006). Induction of pluripotent stem cells from mouse embryonic and adult fibroblast cultures by defined factors. *Cell* 126, 663–676.

Takahashi, K., Tanabe, K., Ohnuki, M., Narita, M., Ichisaka, T., Tomoda, K., and Yamanaka, S. (2007). Induction of pluripotent stem cells from adult human fibroblasts by defined factors. *Cell* 131, 861–872.

Tang, B.L. (2009). Neuronal protein trafficking associated with Alzheimer disease: from APP and BACE1 to glutamate receptors. *Cell Adh. Migr.* 3, 118–128.

Thinakaran, G., and Koo, E.H. (2008). Amyloid precursor protein trafficking, processing, and function. *J. Biol. Chem.* 283, 29615–29619.

Thinakaran, G., Harris, C.L., Ratovitski, T., Davenport, F., Slunt, H.H., Price, D.L., Borchelt, D.R., and Sisodia, S.S. (1997). Evidence that levels of presenilins (PS1 and PS2) are coordinately regulated by competition for limiting cellular factors. *J. Biol. Chem.* 272, 28415–28422.

Vassar, R., Bennett, B.D., Babu-Khan, S., Kahn, S., Mendiaz, E.A., Denis, P., Teplow, D.B., Ross, S., Amarante, P., Loeloff, R., et al. (1999). Beta-secretase cleavage of Alzheimer's amyloid precursor protein by the transmembrane aspartic protease BACE. *Science* 286, 735–741.

Vierbuchen, T., Ostermeier, A., Pang, Z.P., Kokubu, Y., Südhof, T.C., and Wernig, M. (2010). Direct conversion of fibroblasts to functional neurons by defined factors. *Nature* 463, 1035–1041.

Walker, E.S., Martinez, M., Brunkan, A.L., and Goate, A. (2005). Presenilin 2 familial Alzheimer's disease mutations result in partial loss of function and dramatic changes in A β 42/40 ratios. *J. Neurochem.* 92, 294–301.

Yu, J., Vodyanik, M.A., Smuga-Otto, K., Antosiewicz-Bourget, J., Frane, J.L., Tian, S., Nie, J., Jonsdottir, G.A., Ruotti, V., Stewart, R., et al. (2007). Induced pluripotent stem cell lines derived from human somatic cells. *Science* 318, 1917–1920.

Note Added in Proof

While this manuscript was under re-review, another study reporting the generation of hiN cells was published by Pang et al. (2011). Pang, Z.P., Yang, N., Vierbuchen, T., Ostermeier, A., Fuentes, D.R., Yang, T.Q., Citri A., Sebastiano, V., Marro, S., Südhof, T.C., et al. (2011). *Nature*. Published online May 26, 2011. 10.1038/nature10202.